Acta Materialia 230 (2022) 117813

Contents lists available at ScienceDirect

Acta Materialia

journal homepage: www.elsevier.com/locate/actamat

The influence of chemistry on the interface toughness in a WTi-Cu system

Markus Alfreider[a,*], Rishi Bodlos[b], Lorenz Romaner[b], Daniel Kiener[a]

[a] Department Materials Science, Chair of Materials Physics, Montanuniversität Leoben, 8700 Leoben, Austria
[b] Materials Center Leoben Forschungs GmbH, 8700 Leoben, Austria

ARTICLE INFO

Article history:
Received 6 December 2021
Revised 21 February 2022
Accepted 3 March 2022
Available online 5 March 2022

Keywords:
Interface toughness
Thin films
Crack extension
Density functional theory

ABSTRACT

With a considerable amount of commonly used material systems consisting of individual, rather confined layers, the question for mechanical behaviour of their individual interfaces arises. Especially, when considering varying interfacial structures as a result of the processing environment. Furthermore, the interaction between pronounced plasticity and fracture processes can lead to challenges with regards to separation between sole interface- or bulk properties.

The present work investigates the interfacial fracture characteristic of a WTi-Cu sytem commonly found in the microelectronics industry as a heterogeneous model material with pronounced plasticity in the Cu phase. To study this behaviour on a rather limited scale (<6 µm), microcantilever experiments were conducted and evaluated using a continuous J-Δa curve evaluation scheme with classical elastic-plastic considerations in mind. A change in interface chemistry, resulting from air exposure between processing steps, was probed and found to show distinct crack propagation along the interface opposed to crack tip blunting as encountered in the vacuum processed sample. Complementary density functional theory calculations also showed a strong reduction of interface cohesion upon oxygen accumulation and a model framework based on classical dislocation plasticity considerations revealed the transition from plasticity to fracture processes to be a result of shielding and following change in mode mixity.

1. Introduction

A considerable amount of technologically relevant material systems consists of multi-layered structures, where individual constituents meet different demands with regards to, *e.g.* electrical [1,2] or thermal [3–5] insulation/conduction, wear protection [6], semi-conducting [7] or optical properties [8]. These systems are often confined to only a few hundred nm up to tens of µm, which gives rise to significant challenges with regards to evaluation of structural properties. However, as the resulting stresses during service that arise due to thermal conditions and/or external loading are commonly non-negligible, it is necessary to investigate mechanical threshold values, *e.g.* yield onset or critical fracture parameters. First steps to meet these challenges were made in recent years, facilitated by the development of various small scale testing techniques, such as nanoindentation [9,10], micropillar compression [11,12] or microtensile testing [13–15] for plasticity values and notched microcantilever bending [16,17], double cantilever wedging [18] or pillar splitting [19] for fracture toughness values. Especially, microcantilever bending has been successfully applied to a wide field of systems with either spatially limited geometries, *i.e.* thin films [20] or very confined local features of interest, such as grain boundaries [21,22] or interfaces [23–25], to address fracture properties of confined material conditions. However, while most of the recent literature addresses the experimental evaluation within the framework of linear-elastic fracture mechanics (LEFM) [16,26,27], the application of elastic-plastic fracture mechanics (EPFM) [28–30] is only rarely found due to more challenging experimental conditions. Given that a high failure tolerance is generally desired, and many application relevant systems already show pronounced plastic deformation around the fracture process zone, it is necessary to incorporate EPFM into small scale testing, especially if subtle changes of mechanical response due to local fluctuations in chemistry or structure are to be probed.

In the present work, we focus on the fracture characteristics of a WTi-Cu interface in a thin (<6 µm) multilayer system as a universal model system for a heterogeneous interface with significant differences in elastic properties amongst the phases and pronounced plasticity in one of them. The interface was deliber-

* Correspondence author.
E-mail address: markus.alfreider@unileoben.ac.at (M. Alfreider).

https://doi.org/10.1016/j.actamat.2022.117813

ately altered by air exposition between processing steps to induce chemical changes due to oxide formation, leading to a comparative set of samples with and without an interfacial oxide layer, while leaving everything else unaltered. Microcantilever experiments and EPFM evaluation schemes were conducted to investigate the interface fracture properties, and pronounced changes with respect to air exposition were evidenced. In conjunction with density functional theory (DFT) simulations and classical dislocation plasticity considerations, we present a reasoning for the observed behaviour, which we suggest as an explanatory foundation for the general behaviour of elastic-plastic bi-layer materials systems at the micron scale.

2. Experimental

2.1. Materials and sample preparation

The multi-layered material system studied herein is based on common wafer processing technologies and consists of the following constituents: (001) oriented single crystalline Si substrate, 50-70 nm thermally grown SiOx, 270-300 nm WTi layer (~100 nm grain size) and 5 µm electrodeposited Cu film (~2.7 µm grain size). Afterwards the structure was annealed at 400°C for 30 min, which leads to an incorporation of the Cu seed layer into the galvanically deposited film and therefore a homogeneous grain size distribution in the µm regime and no residual obvious texture. This material combination is a common base structure in the microelectronics industry and was studied previously, *e.g.* by Wimmer et al. [31], Bigl et al. [32] (Film A) and Alfreider et al. [33], where further information can be found.

Usually, such specimens are entirely processed in vacuum. However, to obtain a different chemical environment at the interface between WTi and Cu, the specimens were deliberately exposed to atmosphere after the WTi deposition step for a short amount of time (~10 min), which resulted in the formation of an undefined surface oxide layer before Cu deposition was continued. Thus, this layer stack allows the investigation of mechanical differences at the WTi-Cu interface as a consequence of oxygen exposition.

To probe the interface fracture properties of the standard vacuum processed as well as the air-exposed interface, micron sized cantilever shaped specimens were fabricated by focussed ion beam milling (FIB, LEO 1540XB, Carl Zeiss AG, Oberkochen, Germany) on mechanically broken platelets of the multilayer stack as shown in Fig. 1a. First, a smooth 90° corner was fabricated using higher FIB milling currents (10 nA) as shown in Fig. 1b, followed by subsequently decreasing currents down to 50 pA for polishing the final shape as depicted in Fig. 1c. An initial notch a_0 was produced also with 50 pA and positioned manually between the Cu and the WTi layer before the final polishing step to reduce curtaining artefacts.

2.2. Microcantilever fracture experiments and evaluation

All microcantilever deflection experiments were conducted in the same FIB, utilizing a Hysitron PI-85 system (Bruker Corporation, Billerica, USA) equipped with the nanoDMA III upgrade to allow for continuous measurement of stiffness changes during testing. To achieve a line contact between transducer and specimen, a 5 µm wide conductive diamond wedge tip with an opening angle of 60° (Synton-MDP AG, Nidau, Switzerland) was used. The specimens were loaded in open-loop, load-controlled mode with a superimposed sinusoidal amplitude of 5 µN at a frequency of 80 Hz and a nominal loading speed of 10 µN/s, based on previous investigations [30]. To reduce any contact issue with the inherently load-controlled transducer, the specimens were elastically pre-loaded to 10 µN before the start of each experiment.

As the Cu part of the fracture specimen is prone to a major amount of plastic deformation, it is necessary to conduct an elastic-plastic fracture mechanical evaluation based on the *J*-Integral concept, as described in detail in previous works [30,33]. Due to the heterogeneous nature of the specimens it is not possible to apply the common splitting of elastic and plastic components of the *J*-Integral [34,35], as the Young's modulus of the multilayer stack is not properly defined. Therefore, we consider an older calculation for the J-Integral evaluation as [36,37]:

$$J_n = \frac{2A_{tot,n}}{B(W-a_n)} \tag{1}$$

where J_n is the *J*-Integral at point n, $A_{tot,n} = \int_0^{u_n} F\,du$ is the total area under the measured load-displacement (F-u) curve up to point n, a_n is the current crack length at point n and B, W are geometric parameters as defined in Fig. 1c. The current crack length a_n is calculated from the experimentally gathered compliance signal [30] as:

$$\int_0^{a_n} \frac{a}{W} Y\left(\frac{a}{W}\right)^2 da = \frac{\left(\frac{c_n}{c_0}-1\right)L^3}{18\pi\left(1-\nu^2\right)L'^2} \tag{2}$$

where $Y(a/W)$ is a geometry factor [16], $\nu = 0.3$ is Poisson's ratio, c_n is the measured compliance of the cantilever at point n and c_0 is the compliance of the unnotched cantilever. The detailed derivation of Eq. (2) is provided in [38]. The compliance of the unnotched beam is initially unknown, but can be evaluated from the stable compliance level $c(a_0)$ after initial contact is established [30] and before crack extension occurs as [33]:

$$c_0 = \frac{c(a_0)}{1+\frac{18\pi\left(1-\nu^2\right)L'^2}{L^3}\int_0^{a_0}\frac{a}{W}Y\left(\frac{a}{W}\right)^2 da} \tag{3}$$

All integration was done numerically using the trapezoidal rule and the crack length a_n was found by interpolation. Furthermore, as both Eqs. (2) and (3) are independent of any material parameters with the exception of Poisson's ratio, they can be considered applicable for the given heterogeneous material system.

2.3. Density functional theory simulations

As the aim of the DFT calculations was to study the difference of interface cohesion with and without air exposure, it was feasible to simplify the investigated system and reduce computational effort by considering single phase body centred cubic (bcc) W instead of WTi and a single layer of O instead of varying air compositions. While the precise chemical species will locally (atom by atom) have different bonding strengths to Cu, it was found that all common oxides (WO_3, WO_4, TiO_2), some oxidation states which seem to be in between WO_3 and WO_4, as well as carbon-oxygen environments, metal-hydroxyde and metal carbonate environments are all present in roughly equal amounts on the surface of the as deposited WTi surface [39]. Furthermore, even in the vacuum processed state residual oxygen containing states remain [40]. Therefore, the DFT simulations were simplified to systems with and without a single oxygen layer, as a full investigation on all different environments would justify a study of its own, rather than being an explanatory tool in conjunction with experimental results and analytical considerations. The simulation system consisted of 48 W atoms (valence electron configuration: 5p6 5d4 6s2) on top of 60 Cu atoms (valence electron configuration: 3d10 4s1) in a Nishiyama-Wassermann [41,42] configuration (Fig. 2). In the case of the air exposed system a single layer, consisting of 8 O atoms (valence electron configuration: s2 p4) was inserted between the Cu and W slab. The DFT calculation were done for various interface separation distances d, using the Vienna Ab-Initio Simulation

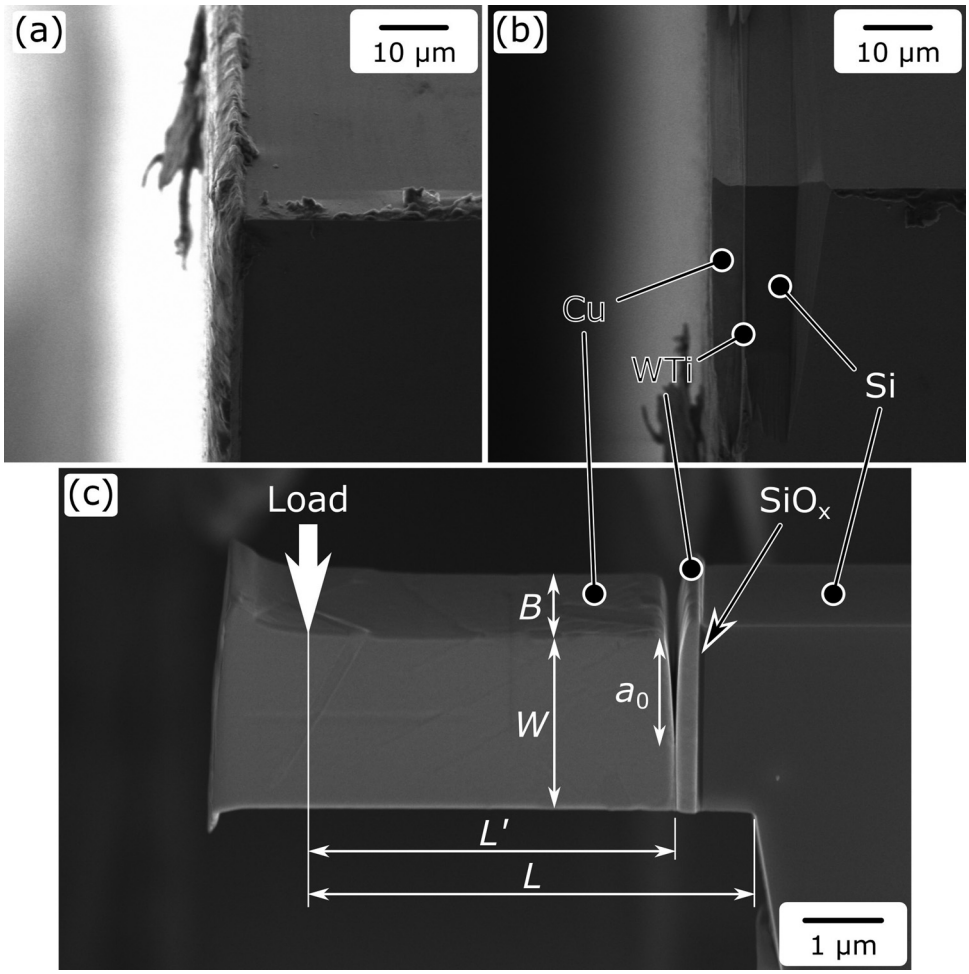

Fig. 1. (a) The 90° corner of an as-broken wafer platelet. (b) The same 90° corner after coarse FIB processing reveals the individual constituents of the multilayer stack. (c) The final shape of a microcantilever specimen on the same corner before testing, with indication of all necessary geometric dimensions for further evaluation.

Package (VASP) [43–45] using Perdew–Burke-Ernzerhof (PBE) functionals [46,47] and the projector augmented wave method (PAW) [48,49]. The KPOINT mesh was 3 × 8 × 1 and periodic boundary conditions were applied in x and y direction (Fig. 2).

The binding energy E_b as a function of d was calculated as:

$$E_b(d) = \frac{E_{sys}(d) - E_{sys'}}{A} \tag{4}$$

With $E_{sys}(d)$ being the energy of the whole system at separation d and $E_{sys'}$ denoting a system with sufficient amount of vacuum between the Cu fcc and W bcc slab to have no remaining interaction ($E_{sys}(d \to \infty)$). In order to probe only the cohesive properties of the interface excluding any elastic contributions from the individual slabs, the individual Cu and W atom positions remained fixed in z direction, while the O atoms were allowed to relax freely after each separation increment. Plotting the binding energy over a large separation range gives us a traction separation curve. A similar, more in depth calculation of traction separation curves with focus on the effect of C impurities on Mo grain boundaries can be found in Ref. [50].

3. Results

The challenging nature of the individual sample preparation on the edges of such platelets does not allow for a large statistical assessment, but rather serves an in depth evaluation of each specimen specifically. Therefore, two specimens of each processing route (full vacuum processing or air exposure) are shown in detail in the following. All geometric parameters were measured before testing using ImageJ 1.54s, with the exception of a_0, which was measured after failure at the fracture surface. Error estimates for all non-specified measurements can be considered as ±30 nm, which corresponds to ±3 px. The error estimates of a_0 are based on the standard deviation of 10 evenly spaced measurements over the whole width of the fracture surface. All data is summarized in Table 1.

3.1. Fracture experiments

The raw load and dynamic compliance data with respect to load-line displacement is given in Fig. 3 for all specimens. Evidently, the vacuum processed specimens (Fig. 3a,b) show only minor decrease in load after the linear elastic regime, while the air exposed specimens (Fig. 3c,d) depict a distinct decrease of load with increasing displacement. This is also represented in the dynamic compliance data (red), where the vacuum processed specimens exhibit a very minor increase in dynamic compliance, which settles after roughly 1000 nm of displacement (Fig. 3a,b), while the dynamic compliance of the air exposed specimens continuously increases with displacement. This difference is specifically apparent as the plotted range of dynamic compliance is 2 nm/µN for the air exposed specimens, whereas it is only 1 nm/µN for the vacuum processed ones. To address whether a systematic influence of difference in sample geometry is present, Fig. 3e shows the conditional stress intensity K [16] of all specimens up to a deformation

Table 1
Geometries of all cantilevers used for evaluation.

	L [µm]	L' [µm]	a_0 [nm]	W [µm]	B [µm]	L'/L	a_0/W	L'/W
vacuum 1	6.79	4.20	1120±252	2.02	1.14	0.62	0.55	2.08
vacuum 2	5.08	4.73	1540±115	2.36	2.22	0.73	0.65	2.00
air 1	4.42	3.67	1410±150	2.31	1.87	0.83	0.61	1.59
air 2	5.81	3.98	900±76	2.19	1.66	0.68	0.41	1.82

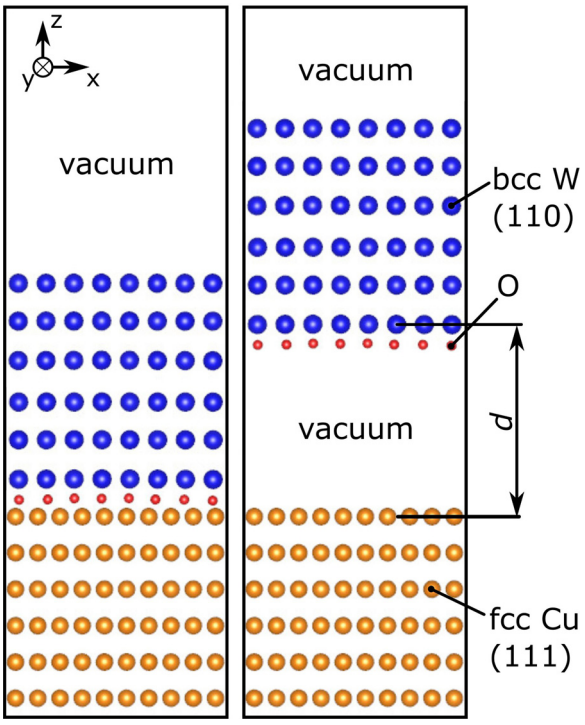

Fig. 2. Simulation system in initial and separated positions. Blue spheres correspond to bcc W atoms, yellow spheres to fcc Cu atoms and the smaller red spheres to O atoms.

of 1000 nm. As K is based only on linear elastic fracture mechanics considerations, it is definitely not valid beyond the elastic loading regime. However, the deviation from the linear elastic slope (onset of plastic deformation or fracture processes) is between 0.7 and 1.4 MPam$^{1/2}$, without any distinct trend between vacuum processed or air exposed specimens. Furthermore, also the stress intensity values after onset of plasticity do not show any specific trend with regards to specimen type, which emphasizes again that no systematic error with respect to specimen geometry is present and that linear elastic concepts are definitely not sufficient to evaluate the given experiments.

The calculated J over crack extension Δa data for all specimen is summarized in Fig. 4a, where the difference between the air exposed and vacuum processed specimens is clearly evident. While the vacuum processed specimens resemble no comparability to the classical concave-down "R"-curve behaviour as observed commonly in fracture mechanical evaluation [51,52], the air exposed specimens depict an evident transition from a similar blunting regime to a nearly linear increase of J with Δa.

Fig. 4b,c show the *in situ* SEM micrographs of the initial and final shape of the second air exposed specimen, respectively. There it is evident that no pronounced crack extension took place. Instead the whole deformation was governed by plasticity in the Cu phase, which is in agreement with the corresponding J-Δa data, where no major crack extension was detected. The initial notch in the first air exposed specimen was fabricated quite far in the Cu phase (~100 nm away from the interface) as seen in Fig. 4d. Nevertheless, after some major amount of plastic deformation a small detachment of the Cu phase from the WTi layer was observed in the *in situ* images (Fig. 4e) up to a final full crack extension in the interface as evident in Fig. 4f. However, correlating the images with the data, one finds that the first occurrence of this detachment is already far into the linear regime of the J-Δa curve, while the transition between blunting and linear regime is considerably earlier at $J = 103.1 \pm 1.8$ J/m^2 (errors are based on the standard deviation of ±100 data points). This leads to the conclusion that the crack did extend in the specimen interior before it was visible on the outer specimen surface. This is also reasonable considering the initial two faster crack extensions ($J = 11.5 \pm 0.3$ and 58.4 ± 2.8 J/m^2) in this specimen as evident in the blunting part of the data (Fig. 4a), as the crack needed to grow towards the interface in the specimen interior before it could grow towards the visible surface. The notch in the second air exposed sample was positioned precisely at the interface (Fig. 4g). However, the transition from blunting to crack extension at $J = 74.3 \pm 0.6$ J/m^2 as depicted in Fig. 4h is again not evident. Even far in the linear regime the *in situ* images still show a major amount of crack tip blunting without any evident surface crack extension (Fig. 4i). Only at a crack extension of 526 nm did it grow large enough to create a visible interface detachment (Fig. 4j) up to a nearly complete detachment of the Cu phase from the WTi layer (Fig. 4k), while still a lot of plastic deformation in the Cu was evident.

To visualize the difference between the two interface states in more detail, Fig. 5 shows the *post mortem* fracture surface of a vacuum processed and an air exposed specimen in comparison. The specimens were bent down further after the experiments to better expose the fracture surfaces, and the images are taken under an angle of 30°. The vacuum processed specimen (Fig. 5a) shows no distinct extension of the crack from the initial notch, while the air exposed specimen (Fig. 5b) clearly depicts a surface pattern on the WTi side, which appears imprinted as a negative on the Cu side. These surface patterns are resultant of the faceted WTi layer, as shown for comparison in Fig. 5c in pristine condition before any further deposition took place. It is likely that the faceted nature of the WTi surface acts as superimposed stress concentrators on top of the initial FIB induced notch, which suggests that locally the threshold for crack extension can be overcome rather easy.

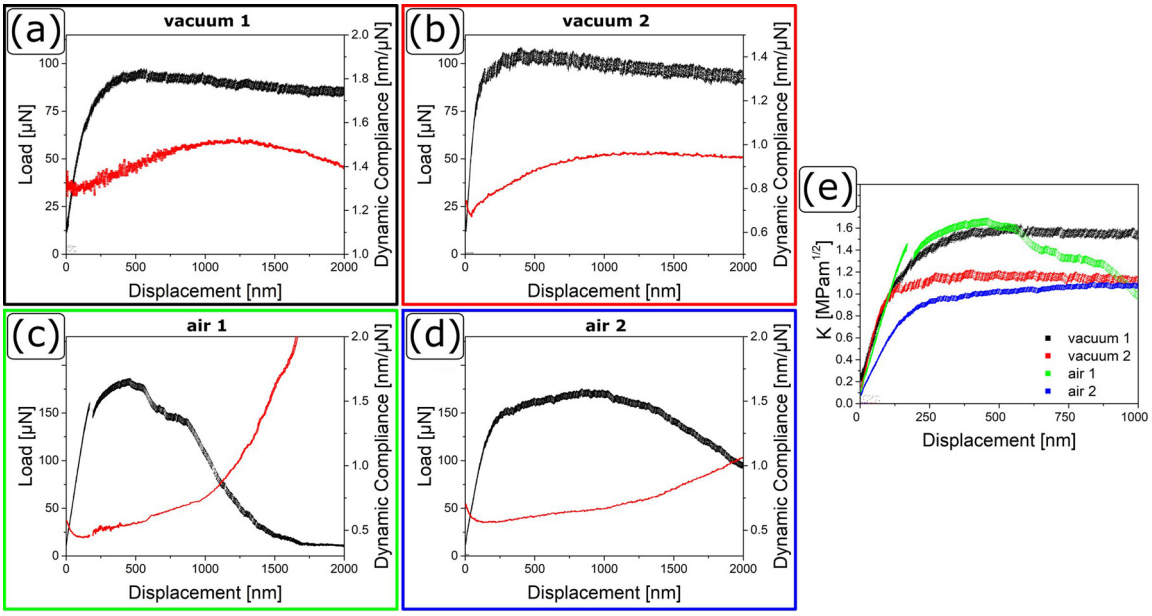

Fig. 3. Raw load-displacement (black) and dynamic compliance-displacement (red) data of (a,b) the two vacuum processed specimens and (c,d) the two air exposed specimens. (e) The conditional stress intensity of all specimens shows a deviation from the linear elastic regime between 0.7 and 1.4 MPam$^{1/2}$, without any trend with respect to processing conditions.

Taken together, these observations are a strong evidence that the crack grew explicitly at the interface between the layers, as this very detailed pattern still remains intact on both sides of the cantilever (Fig. 5b).

3.2. Atomistic interface binding energy

The results of the DFT simulations are summarized in Fig. 6a, where the binding energy E_b as a function of interface separation d of the W/Cu system and the W/O/Cu system are depicted as blue filled circles and orange open squares, respectively. To investigate the traction-separation behaviour of the two interface states the universal binding energy relation (UBER) fit, proposed by Rose et al. [53] was utilized as:

$$E_b = -E_{b,max}\left(1+\frac{d}{l}\right)e^{-\frac{d}{l}} \tag{5}$$

where $E_{b,max}$ is the largest absolute value of the potential well, commonly also referred to as "Work Of Separation" (WOS), and l is a fitting parameter, commonly correlated with the Thomas-Fermi screening length [53,54]. The non-linear least-square fitting procedure was conducted using the lmfit package (version 1.0.0) within the Python programming environment (version 3.7.7). The derivation of E_b with respect to d gives the traction σ perpendicular to the interface, necessary to pull it a distance d apart, as shown in Fig. 6b. It is evident from the peak heights that an approximately six times higher normal stress would be necessary in the pure W/Cu system compared to the W/O/Cu system to pull the interface apart. It should be noted that both the vacuum processed as well as the air exposed systems have a considerably lower WOS than individual W grains (6-7 J/m^2) [55], calculated with the same method, which further supports the indication that any crack would grow along the interface. Furthermore, the respective peak positions δ show that the point at which the separation becomes unstable for a given stress is reached earlier ($\delta_{W/O/Cu}$ = 42.5 pm) in the oxygen containing system than in the pristine system ($\delta_{W/Cu}$ = 56.5 pm). All calculated values are summarized in Table 2.

Table 2
Calculated parameters based on the DFT simulations for the W/Cu and W/O/Cu system, respectively.

	$E_{b,max}$ (WOS) [J/m^2]	σ_{max} [GPa]	δ [pm]
W/Cu	3.471	22.67	56.5
W/O/Cu	0.429	3.72	42.5

4. Discussion

Based on the experimental data there is little doubt that the air exposure has a very strong influence on the fracture behaviour of the WTi-Cu interface. While both processing states show a major amount of plastic deformation in the initial loading, the air exposed specimens failed by nucleating and extending a crack at the interface, which was not observable in the vacuum processed samples. This suggests a different threshold for the accumulation of crack tip plasticity before fracture processes occur. To rationalize the observed behaviour, we will on the one hand take a detailed look at the crack tip-dislocation nucleation interaction model proposed by Jokl et al. [56]. On the other hand, we will regard the change in local stress fields due to piling-up of dislocations (as a substitute for the global accumulation of plasticity) and conclude that while both models are in reasonable agreement, the pile-up model suggests a change in mode mixity with increasing plasticity which better elucidates the transition from deformation to crack extension.

4.1. Crack extension vs. dislocation nucleation

The commonly applied Orowan modification [57] to the classical Griffith criterion [58] states that:

$$G_c = 2\gamma + \gamma_p \tag{6}$$

where G_c is the critical energy release rate to extend a crack, γ is the surface energy and γ_p is the dissipated work during the process, *e.g.* plasticity or phase transformation. Usually γ_p is considered a scalar material specific parameter. However, in 1980 Jokl et

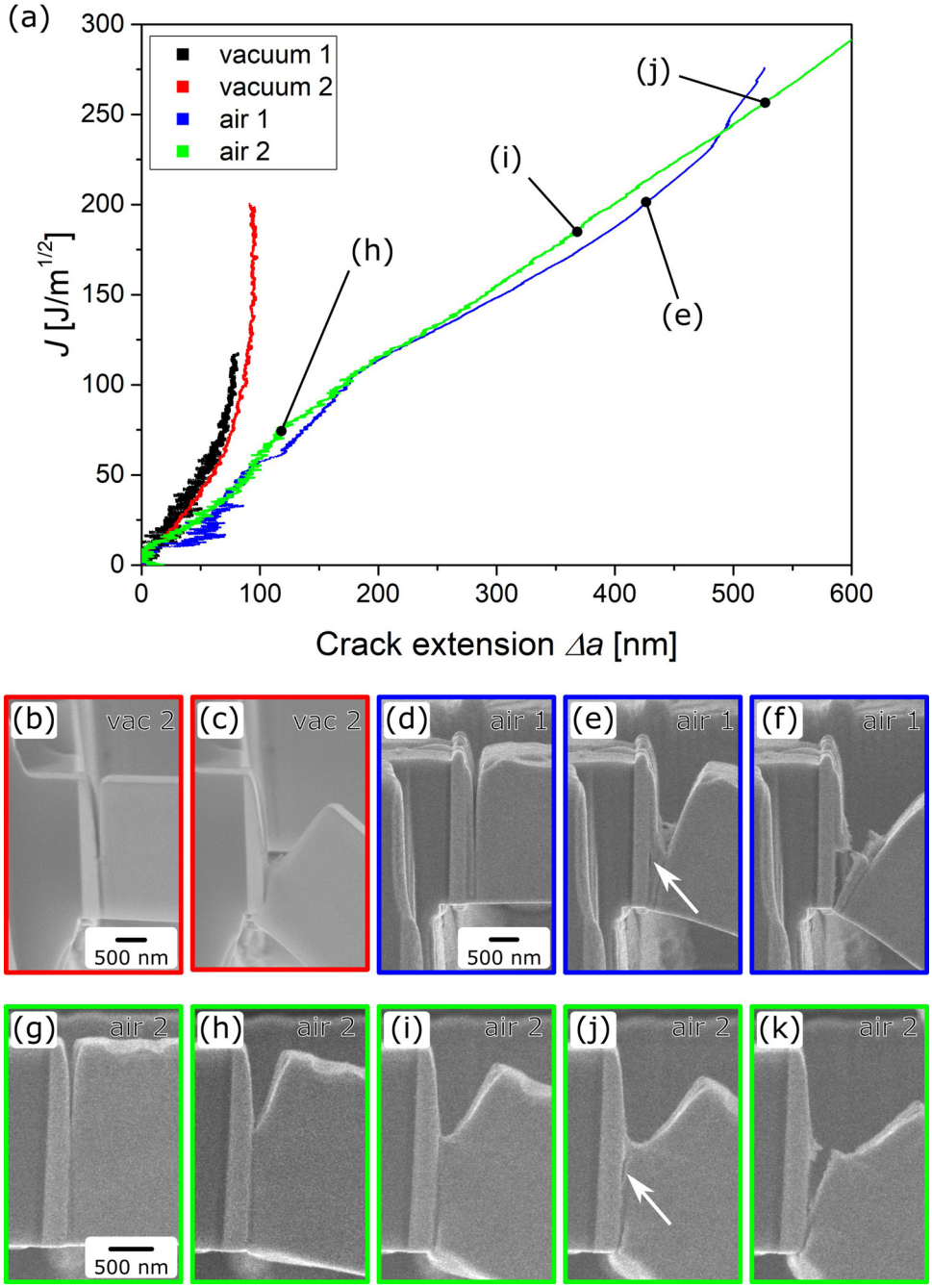

Fig. 4. (a) J-Δa curves of all specimen, showing a distinct difference between the vacuum processed and air exposed versions. *In situ* SEM images showing the (b) initial and (c) final shape of a vacuum processed specimen and the evolution of crack geometry of the (d-f) first and (g-k) second air exposed specimen with notches close to and exactly at the interface, respectively.

al. [56] argued that instead of a scalar value, γ_p should be considered as a function of γ as well, due to the fact that generally observed embrittling phenomena based on segregation, *e.g.* P in steels [59], S in Cu [60], would not affect dislocation mobility but rather cohesion and therefore γ. Their basic assumption is that dislocation emission and crack extension are simultaneous events, which leads to the mechanistic second order differential equation of motion as:

$$m\ddot{x} = -\frac{4\gamma b^2}{\delta^2}x + b^2\tau(\nu_0, n, G, k, t) \tag{7}$$

where m is the mass of a single atom, x is the displacement perpendicular to the crack plane, b is the magnitude of the Burger's vector, δ is the critical separation distance (see Table 2) and τ is the shear stress along the crack plane as a function of terminal dislocation velocity v_0, velocity exponent n, shear modulus G, local stress intensity k and time t. A schematic of the crack tip structure for this model is shown in Fig. 7a. Solving Eq. (7) for different values of k and searching for the first time at which $x>\delta$ leads to a function of the bond breaking time $t_B(k)$. From this, one can calculate the resulting work of dislocation emission $w_p(\gamma,k)$ up to time $t_B(k)$, and with that and the thermodynamic criterion:

$$-\frac{k^2}{2G}(1-\nu) + 2\gamma + w_p(\gamma, k) \leq 0 \tag{8}$$

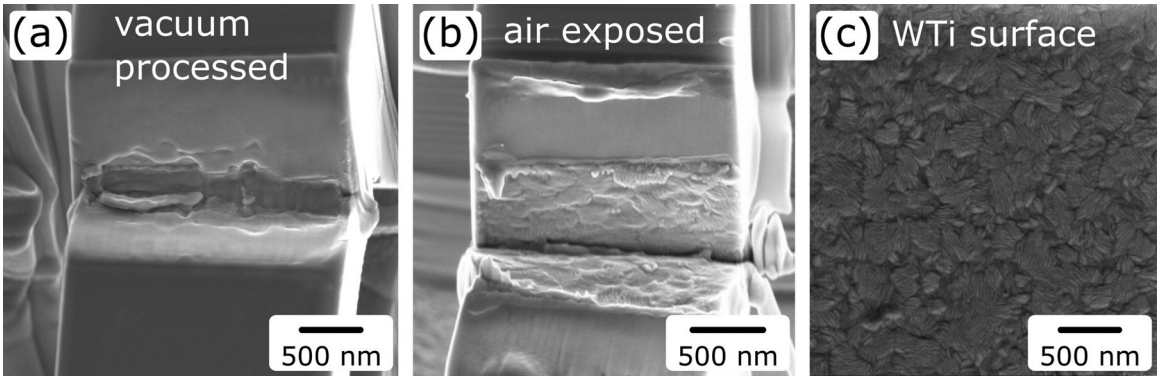

Fig. 5. SEM micrographs of the fracture surfaces of (a) a vacuum processed and (b) an air exposed specimen. (c) The plain WTi surface without any further deposited layers.

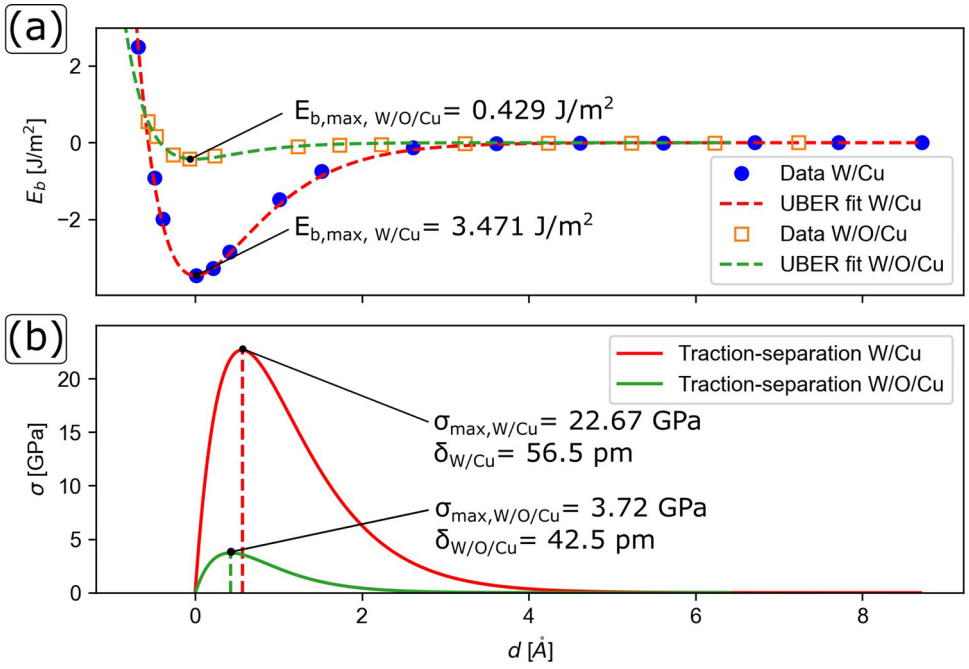

Fig. 6. (a) Binding energy as a function of interface separation for the W/Cu interface (blue dots) and the W/O/Cu interface (orange squares) with the corresponding UBER-fits as dotted lines (red, green). (b) The traction-separation relations for both interfaces.

find the local stress intensity upon fracture k_G. The plastically dissipated energy as a function of surface energy is then $\gamma_p(\gamma) = w_p(\gamma,k_G)$. The detailed derivation of all given formulae is not in the focus of this investigation and would exceed the present manuscript, but the interested reader is encouraged to read Jokl et al.'s original work [56].

The given mathematical framework was solved numerically for Cu considering a full ⟨110⟩{111} dislocation (b = 256 pm) instead of partials, with a terminal dislocation velocity v_0 = 1600 m/s [61,62] and a velocity exponent n = 1.8 [63]. The calculations were conducted using the LSODA algorithm [64] within the scipy library (version 1.2.1) using Python 3.7.7, with the boundary conditions of the differential Eq. (7) (initial position x_0, initial velocity $\dot{x}_0$) set to 0.

The k_G (half symbols) and resulting γ_p (filled/open symbols) values were calculated as functions of the work of separation in 0.1 J/m^2 steps for both critical separation distances $\delta_{W/Cu}$ = 54.5 pm and $\delta_{W/O/Cu}$ = 42.5 pm, respectively, and are shown in Fig. 7b. There, it is evident that the W/Cu system has a steeper increase in plastic dissipation and an earlier point at which no bond breaking can be detected (2.7 J/m^2), in comparison to the W/O/Cu system where the bond breaking becomes undetectable at 4.3 J/m^2. This occurs due to the fact that the thermodynamic criterion becomes non-negative over the whole k-range, which means that dissipated energy by dislocation emission dominates over the released energy by crack extension. Comparing this with the work of separation (WOS) from the DFT calculations (dotted lines), one finds that for the pure W/Cu system the point at which no bond breaking can be detected is far below $WOS_{W/Cu}$, suggesting that only dislocation plasticity and no crack extension would take place, while in the W/O/Cu system the point at which bond breaking terminates is far above $WOS_{W/O/Cu}$, which means that both plasticity and fracture processes are occurring.

However, the quantitative values should be taken with care, as in this model the amount of plastic dissipation would only be roughly 0.4 J/m^2, which results in a critical J-integral value for crack initiation of $J_i \approx 0.8$ J/m^2 for the air exposed specimens, while we find values of up to J_i = 103.1 J/m^2 (Fig. 4a). This discrepancy of over two orders of magnitude is a result of considering only the very near crack tip region with rather simplified assumptions, *e.g.* neglecting crystallography, thermal activation, dislocation splitting or cross slipping. Nevertheless, although we only consider the Cu phase for the calculation of plasticity-fracture process interactions, the model gives an astonishing qualitative agreement with

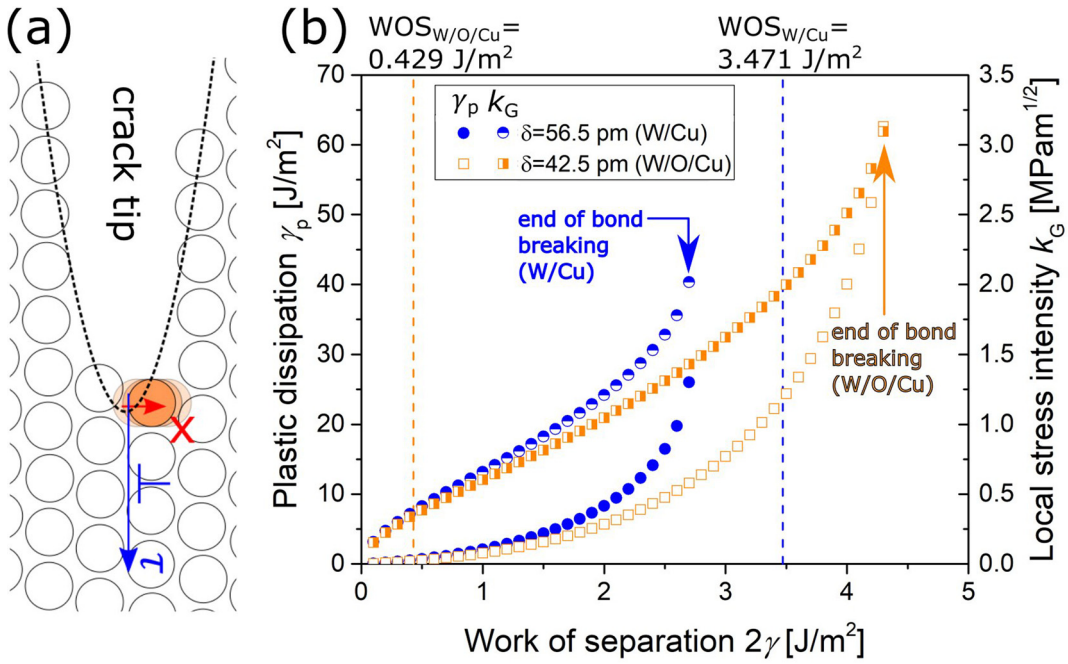

Fig. 7. (a) Schematic of the atomistic crack tip model depicting the perpendicular deflection x and the direction in which the dislocation emitting shear stress τ is acting. (b) Calculated plastic dissipation γ_p and local stress intensity for unstable fracture k_G over work of separation 2γ for the W/Cu and W/O/Cu system, respectively. The last point at which bond breaking occurs is depicted for both models. At higher WOS only dislocation emission takes place.

the experimental data, where again the vacuum processed specimens (correlate to W/Cu) show only plastic deformation, while the air exposed specimens (correlate to W/O/Cu) show both, plasticity and crack extension.

4.2. Dislocation activity prior to crack extension

As the air exposed specimens do not show an initially brittle behaviour, but rather a distinct transition from plastic deformation to crack extension, it can be argued that this initial accumulation of plasticity creates an essential change to the specimen structure, which subsequently enables the fracture process. The most straightforward explanation is that continuous dislocation nucleation would lead to classical forest hardening, which inhibits subsequent nucleation and leads to an increased threshold for plasticity. However, in specimens as small as the present ones, the necessary dislocation entanglements would be limited to a very confined volume, which means they need to remain in the near vicinity of the crack tip (<1 µm). Independent on how these dislocations arrange, such a high density of dislocations close to the crack tip would lead to a shielding effect on the crack tip and further to a reduced local stress intensity [65,66]. Given that such an accumulation would reduce both, the driving force for dislocation plasticity as well as for crack extension, it is difficult to understand at which point one overtakes the other (in the case of the air exposed specimens) if such a point even exists (considering the vacuum processed specimens).

Thus, in the following we will present a 2-dimensional model based on piling up of edge dislocations in front of the crack tip and investigate the resulting local shielding behaviour. All geometric arguments will be presented in a r,Θ-polar coordinate system as common in fracture studies, with $r = 0$ at the crack tip and $\Theta = 0$ along the WTi-Cu interface (Fig. 8a, shown representatively for the 8th dislocation).

Consider a single slip plane in the Cu phase under an angle Θ that passes through the crack tip. Neglecting the actual nucleation process at the crack tip and any subsequent cross-slip or climb mechanisms, the force equilibrium along the slip plane of the i-th dislocation in a pile-up of n dislocations is [67,68]:

$$b\tau_i = F_{image} + F_{crack} + \sum_{\substack{m=1 \\ m \neq i}}^{n} F_d^m \tag{9}$$

where τ_i is the total shear stress acting on the i-th dislocation (classical Peach-Koehler force $F_i = b\tau_i$ [69]), F_{image} is the image force, F_{crack} is the force resulting from the stress field of the loaded crack and F_d^m is the force resulting from the stress field of the m-th dislocation acting on the i-th dislocation. Finding these force components is rather challenging due to the fact that the present study focuses on a heterogeneous material system. This leads to the fact that the local stress fields are not static, but a function of the elastic mismatches between the constituents and are changing with respect to the point of investigation as the point-specific mode I (k_I) or mode II (k_{II}) components change. This is known as an oscillatory singularity and the detailed derivation is beyond the scope of this work, but the interested reader is referred to a very thorough review by Hutchinson and Suo [70]. For the sake of conciseness, we will be taking the fact that the mode mixity angle ψ is a measure for the ratio between local mode I and mode II loading ($\tan(\psi) = k_{II}/k_I$) and that it is given by:

$$\psi = \arctan\left(\frac{Im\left(Kl^{i\varepsilon}\right)}{Re\left(Kl^{i\varepsilon}\right)}\right) \tag{10}$$

where $K = K_1 + iK_2$ is the complex loading stress intensity factor, $\varepsilon = \frac{1}{2\pi} ln(\frac{1-\beta}{1+\beta})$ is a function of the second Dundurs' parameter β [71] and therefore the individual shear moduli and Poisson's ratios G_W = 157 GPa, ν_W = 0.28 [72] and G_{Cu} = 45 GPa, ν_{Cu} = 0.35 [73], and l is an arbitrary reference length. The elastic parameters are taken for W instead of WTi for a better comparison with the DFT results. For simplification it is further assumed

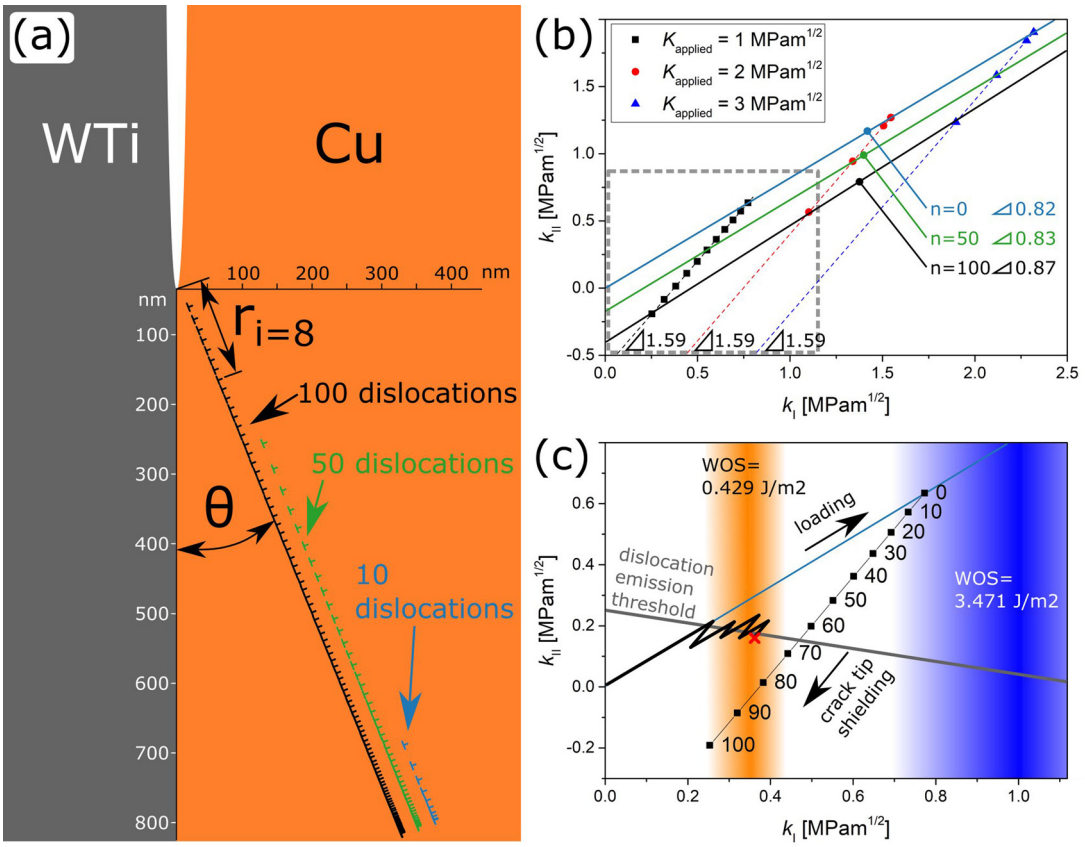

Fig. 8. (a) Schematic interface crack tip showing the dislocation distribution for n = 10, 50, 100 dislocations on a slip plane at $\Theta = 22°$, where the last dislocation is pinned at r = 880 nm. (b) Local k_I and k_{II} stress intensities for a shielded crack with varying applied stress intensities $K_{applied}$ = 1, 2, 3 MPam$^{1/2}$ and for varying amounts of dislocations (n = 0-100) in the pile-up. (c) Detail of grey region in (b) showing the loading slope, dislocation emission threshold and respective crack growth thresholds after Lin and Thomson [80].

that the applied loading is purely mode I, *i.e.* has only a real component $K_{applied} = K_1$. With these assumptions and the radial shear stress solutions for mode I $\tau_{r\Theta,I}$ and mode II $\tau_{r\Theta,II}$ [52,74,75], F_{crack} equates to:

$$F_{crack} = b(\tau_{r\Theta,I} + \tau_{r\Theta,II}) = b\frac{K_{applied}}{\sqrt{2\pi r}}\cos\left(\frac{\Theta}{2}\right)\left[\cos\left(\varepsilon \ln(l)\right)\ \sin\left(\frac{\Theta}{2}\right)\cos\left(\frac{\Theta}{2}\right) + \sin\left(\varepsilon \ln(l)\right)\left(1 - 3\sin^2\left(\frac{\Theta}{2}\right)\right)\right] \quad (11)$$

As the full generalized treatment of the following will lead to a very exhausting and incomprehensible set of interactions, we will at this point specify the characteristic reference length as l = 820 nm (the ligament length of the second air exposed specimen), which leads to a maximum of F_{crack} at $\Theta \approx 22°$(Fig. 8a) and further consider only this slip plane. The image forces on a dislocation in the vicinity of a crack are also more complicated when an interface is involved, as an additional term perpendicular to the interface is introduced. Zhang and Li [76] have derived a full framework for the stress field of an edge dislocation in the vicinity of a crack tip at a bi-material interface based on Muskhelishvili's complex potential treatment [77]. They found that considering an edge dislocation within the Cu phase and a Burger's vector parallel to the slip plane the image force F_{image} is:

$$F_{image} = \left[\left(\frac{\alpha+\beta^2}{1-\beta^2}\frac{G_{Cu}}{4\pi(1-\nu_{Cu})}\right) - \frac{G_{Cu}G_W}{2\pi}\left(\frac{1}{G_{Cu}+G_W(3-4\nu_{Cu})} + \frac{1}{G_W+G_{Cu}(3-4\nu_W)}\right)\right]\frac{b^2}{r} \quad (12)$$

where α is Dundurs' first parameter [71].

Furthermore, the individual dislocation interaction forces F_d^m can be calculated using the same potential method [76]. The detailed derivation can be found in Appendix A, to continue with the argument from this point onwards. With all terms known in Eq. (9) it is now possible to calculate the acting shear stress τ_i of any i-th dislocation in a pile-up in front of the crack tip. This enables the calculation of the actual distribution of dislocations by iteratively moving the individual dislocations along the slip plane until the resolved shear stress drops below the lattice friction, which is taken to be the Peierls-Nabarro stress [78], τ_p = 0.28 MPa for Cu [79]. One can now argue that at some point the interaction of dislocations with each other or with occurring grain boundaries leads to a pinning of these dislocations, which creates a barrier for further dislocation motion. To obtain a lower bound estimate for the resulting pile-up behaviour, we kept the furthest dislocation sessile at a maximum distance of 820 nm/cos(Θ) = 880 nm (as if the pinning point would be as close to the lower free Cu surface as possible), while all other dislocations where allowed to move, starting from an evenly spaced distribution of dislocations. As the bending of the cantilever would lead to a transition from tension to compression, the maximum distance would be definitely shorter than the 880 nm. However, due to the superposition of the crack

tip field and the bending field an exact calculation of the position of the neutral fibre is far from trivial.

The equilibrium positions of the individual dislocations are shown in Fig. 8a for $K_{applied} = 1$ MPam$^{1/2}$ and $n = 10$, 50 and 100 dislocations, respectively. It is evident from the fact that the shortest pile-up ($n = 10$) is condensed at the furthest possible position that without any pinning the driving force from the loaded crack would move them even further away from the tip. However, with a pinning point a number of $n = 100$ dislocations leads to a nearly completely filled slip-plane up to the crack tip. With the actual equilibrium positions of the dislocations now known, one can estimate the local shielded crack tip stress intensities $k_{I,shield}$, $k_{II,shield}$, as [80]:

$$k_{j,shield} = k_j - \sum_{i=0}^{n} k^i_{j,dislocation} \tag{13}$$

where j = I,II and $k^i_{j,dislocation}$ are defined in Appendix B.

The shielded stress intensity is depicted in Fig. 8b in k_I-k_{II} space for varying applied stress intensities $K_{applied}$ = 1,2,3 MPam$^{1/2}$ and various numbers of dislocations, respectively. From there it is evident that the shielding effect is stronger for mode II than for mode I and independent of $K_{applied}$, as the slopes of all points for a given $K_{applied}$ are equally 1.59. Similarly, the slopes for a given number of dislocations are nearly constant with only a very minor increase from 0.82 ($n = 0$) to 0.87 ($n = 100$). This means that, while constant loading increases k_I faster than k_{II}, constant dislocation emission on the other hand decreases k_{II} faster than it decreases k_I. This holds true for shorter lengths of the dislocation pile-up, *e.g.* smaller grains or neutral bending fibres, as a shorter length only lowers the amount of dislocations in the pile-up at which a certain shielding stress is active. Therefore, all conclusions with regards to mode mixity in the simplified tensile stress field assumption remain valid also for a more complex bending stress field.

Lin and Thomson developed a framework for comparison of dislocation emission with cleavage under general loading [80], and from there one finds a threshold for dislocation emission as a line intersection between k_{Ie} and k_{IIe} (neglecting k_{III}), with:

$$k_{Ie} = \frac{G_{Cu} b}{(1-\nu_{Cu})\sqrt{2\pi r_0}} \left(\sin(\Theta) \cos\left(\frac{\Theta}{2}\right) \right)^{-1}$$

$$k_{IIe} = \frac{G_{Cu} b}{(1-\nu_{Cu})\sqrt{2\pi r_0}} \left(2\cos\left(\frac{3\Theta}{2}\right) + \sin(\Theta) \sin\left(\frac{\Theta}{2}\right) \right)^{-1} \tag{14}$$

There, r_0 is the dislocation core cut-off radius commonly approximated by $r_0 = b$ [81,82], which leads to k_{Ie} = 1.204 MPam$^{1/2}$ and k_{IIe} = 0.253 MPam$^{1/2}$ for the given system, respectively. Lin and Thomson furthermore argued that based on the differences in theoretical strengths of materials in tension and shear, the major contribution to cleavage should be due to mode I loading, which leads to the simple approximation:

$$k_{Ic} = \sqrt{\frac{2E\gamma}{(1-\nu^2)}} \tag{15}$$

for a threshold to crack extension. Given that our crack is in the interface, it is not entirely clear whether to use $E = E_{Cu}$ = 124 GPa, $\nu = \nu_{Cu}$ = 0.35 [73] or to use $E = E_W$ = 403 GPa, $\nu = \nu_W$ = 0.28 [72] for evaluation. Therefore, it is reasonable to consider a range, rather than a single value, which leads to $k_{Ic,W/O/Cu}$ = 0.242-0.436 MPam$^{1/2}$ for the oxygen containing system and $k_{Ic,W/Cu}$ = 0.688-1.240 MPam$^{1/2}$ for the pristine system.

Fig. 8c depicts the dislocation emission threshold (gray line), the two crack extension threshold regimes (orange-W/O/Cu, blue-W/Cu) and the pure elastic loading without any shielding (pale blue line) in conjunction with the shielded values for $K_{applied} = 1$ MPam$^{1/2}$ (black squares, numbers correspond to n). To elaborate on what happened in the experiment one can now artificially increase $K_{applied}$ in the graph as follows. The specimen is initially loaded along the pale blue line (slope 0.82), until it reaches the dislocation emission threshold, where dislocations nucleate and start shielding the crack tip (slope 1.59) until it drops below the emission threshold again. This process does not have to be regular, but can be stochastic due to dynamic dislocation emission effects [83]. However, with continued loading it will repeat and move the local stress intensity in close proximity to the dislocation emission line up to a point where it drops below the emission threshold, but is above the threshold for crack extension (Fig. 8c, black zig-zag line to red cross). Thus, changing the behaviour from pure dislocation plasticity, through an intermediate regime where both processes can occur, as indicated by the interplay between crack extension and plasticity in the blunting regime of the first air exposed specimen (Fig. 4), to crack extension.

To establish a link to the J-integral evaluations, one can calculate the plastically dissipated work during the process by summing up the work done by each individual moving dislocation. However, this would lead to a full simulation type approach with regards to time and amount of dislocation nucleation. Nevertheless, we can estimate the magnitude of the plastically dissipated work from the given static data by considering that geometrically adding all of the individual loading segments followed by all the unloading segments leads to a triangle with an endpoint above the crack extension threshold, but below the dislocation emission threshold, similar to the triangle in Fig. 8c drawn by the loading slope and the shielding data for $K_{applied}$ = 1MPam$^{1/2}$. There, the first point below the dislocation emission line is $n = 70$, and the sum of the dissipated work of all 70 dislocations moving from the crack tip to their respective positions normalized by their distance from the crack tip is:

$$J_{diss} = \sum_{i=0}^{n=70} \frac{b}{r_i} \int_0^{r_i} \tau_i(r)\, dr \tag{16}$$

where τ_i is the shear stress calculated by Eq. (9), but taking only into account the dislocations which were emitted before the i-th dislocations (from i+1 to n). Calculating this quantity for $n = 70$ equals $J_{diss,n=70}$ = 6.14 J/m^2 when considering only a single slip plane with a pile-up that begins with the first emitted dislocation, which is an order of magnitude larger than obtained with Jokl et al.'s model [56], while still lower than the experimentally observed J = 74.3 J/m^2. However, such a single pile-up is very unlikely to occur, as many dislocations would move out of the free surface at the bottom of the Cu phase [84] before an event occurs that would lead to dislocation entanglement, *e.g.* jog formation, to initiate a pile-up behaviour. Furthermore, as differently oriented grains exist in the Cu phase, the actual crystallographic orientation of individual slip planes could lead to different behaviour, inhibiting the change in mode mixity (position in k_I-k_{II} space) necessary to initiate crack extension. All of these very likely processes would add to the dissipated work, which means that $J_{diss,n=70}$= 6.14 J/m^2 is only a lower bound estimate. Comparing the air exposed with the vacuum processed specimen in the light of this argument one could think that even the vacuum processed specimen should show crack extension given enough dislocation accumulation. Therefore, one can use the same geometric consideration as before, *i.e.* shifting the loading line and the crack tip shielding line parallel to intersect with the first point at which crack extension should occur for the

W/Cu specimen ($k_I = 0.688$ MPam$^{1/2}$; $k_{II} = 0.108$ MPam$^{1/2}$). The intersection points of these shifted lines with the original ones allow to read out the necessary applied stress intensity $K_{applied} = 1.66$ MPam$^{1/2}$ and amount of dislocations $n \approx 118$ for fracture to occur in the W/Cu specimen. However, when taking a detailed look at the equilibrium dislocation spacing after iterative relaxation for these values, one finds that the distance between the last two dislocations drops below the magnitude of the Burger's vector b, which is physically impossible and suggests that the model breaks down at that point. As a matter of fact, this behaviour starts already with $K_{applied} = 1$ MPam$^{1/2}$ and $n = 80$, which gives reason to assume that the W/O/Cu system is at the very brink of physically possible crack extension, resultant of accumulation of dislocation plasticity.

Nevertheless, this simplified model mimics the observed behaviour very closely and suggests that the accumulation of plasticity in these specimens leads to a change in mode mixity towards a relatively higher mode I component, which facilitates crack extension over dislocation nucleation.

5. Summary and conclusion

Micromechanical cantilever fracture experiments have been conducted on a Cu-WTi-SiOx-Si multilayer stack with the focus on analysing the interface between the plastically deforming Cu phase and the quasi-elastic WTi layer. To address the influence of interface chemistry, one set of specimens was deliberately exposed to air between the deposition steps of the two constituents, which led to the formation of an undefined interface oxide layer. While the standard vacuum processed samples showed only plastic deformation in the Cu phase without any crack extension along the interface, the air exposed specimens exhibited evident crack extension after an extended plastic regime. Continuous J-Δa curves depict a very distinct transition from a concave upwards crack tip blunting to a linear crack extension behaviour, with an onset J-integral value of $J = 74.3 \pm 0.6$ J/m^2 and $J = 103.1 \pm 1.8$ J/m^2 for the two air exposed specimens, respectively. Complementary DFT simulations of a W/Cu interface revealed that upon introduction of a single layer of oxygen the work of separation of the interface drops by a factor of eight from $WOS_{W/Cu} = 3.471$ J/m^2 to $WOS_{W/O/Cu} = 0.429$ J/m^2. Independent of whether the nucleation of dislocations opposed to crack extension or the change in local mode mixity as a result of dislocation pile-ups is considered, the higher work of separation in the pristine interface suggests that static crack extension is impossible in this system. However, the reduced work of separation through oxygen exposition leads to physically plausible results in both model assumptions. Given that the crack extension in the air exposed specimens is preceded by a non-negligible amount of plastic deformation, the argument based on accumulation of dislocation plasticity, leading to a change in local mode mixity towards a relatively higher mode I component (opening mode) seems to be the more probable case for the change from dislocation mediated plasticity to crack extension along the interface.

To conclude, the presented experimental approach on elastic-plastic fracture mechanics on spatially limited structures, *i.e.* thin films, was able to resolve changes in interface toughness in a heterogeneous system due to chemical differences. While one constituent showed a major amount of plastic deformation, the technique was still able to detect crack extension even before it was evident in the *in situ* SEM images. In conjunction with the DFT results and analytical arguments, this provides a quite complete picture of the occurring plasticity-fracture process interactions in the given system, which can act as a starting point for further investigations on similar elastic-plastic material combinations, *e.g.* thermal barrier-, wear- or bio-functional coatings.

Declaration of Competing Interest

The authors declare that they have no known competing financial interests or personal relationships that could have appeared to influence the work reported in this paper.

Acknowledgement

The authors gratefully acknowledge the financial support under the scope of the COMET program within the K2 Center "Integrated Computational Material, Process and Product Engineering, IC-MPPE" (Projects A2.12). This program is supported by the Austrian Federal Ministries for Transport, Innovation and Technology (BMVIT) and for Digital and Economic Affairs (BMDW), represented by the Österreichische Forschungsförderungsgesellschaft (Funder ID: 10.13039/501100004955), and the federal states of Styria, Upper Austria, and Tyrol. This project has received funding from the European Research Council (ERC) under the European Union's Horizon 2020 research and innovation programme (Grant No. 771146 TOUGHIT).

Appendix A

The force acting on the i-th dislocation by the m-th dislocation on a glide plane $F_d{}^m$ is a result of the magnitude of the stress field of the m-th dislocation at the position of the i-th dislocation, as $F_d{}^m = \sigma_{r\Theta}(z_i,z_m)/b$. There, $\sigma_{r\Theta}(z_i,z_m)$ is the resulting shear stress along the glide plane in polar coordinates as a function of the positions of the individual dislocations z_i,z_m. In a two dimensional model these positions can be addressed by complex numbers ($z = x+iy$), which enables the use of Muskhelishvili's complex potential approach [77], leading to:

$$\begin{aligned}\sigma_{rr} + \sigma_{\Theta\Theta} &= 2\left[\phi'(z_i,z_m) + \overline{\phi'(z_i,z_m)}\right] \\ \sigma_{\Theta\Theta} + i\sigma_{r\Theta} &= \phi'(z_i,z_m) + \overline{\phi'(z_i,z_m)} + \left[\overline{z_i}\phi''(z_i,z_m) + \psi'(z_i,z_m)\right]e^{i2\Theta}\end{aligned} \tag{A1}$$

where ϕ and ψ are two complex potentials, the prime denotes differentiation by z_i and the bar denotes complex conjugation. The potentials for dislocations in the vicinity of an interface have been developed by Zhang and Li [76] and the respective derivations for the given system and both dislocations inside the Cu phase are:

$$\phi'_{Cu} = \frac{1}{1-\beta^2}\left[\left(1-\beta^2\right)\frac{\gamma_{Cu}}{z_i - z_m} + (\alpha-\beta)(1-\beta)\left[\frac{\gamma_{Cu}}{z_i - \overline{z_m}} - \overline{\gamma_{Cu}}\frac{\overline{z_m} - z_m}{(z_i - z_m)^2}\right]\right] \tag{A2}$$

$$\phi''_{Cu} = \frac{1}{1-\beta^2}\left[\left(1-\beta^2\right)\frac{-\gamma_{Cu}}{(z_i - z_m)^2} + (\alpha-\beta)(1-\beta)\left[\frac{-\gamma_{Cu}}{(z_i - \overline{z_m})^2} + 2\overline{\gamma_{Cu}}\frac{\overline{z_m} - z_m}{(z_i - z_m)^3}\right]\right] \tag{A3}$$

$$\begin{aligned}\psi'_{Cu} = \frac{1}{1-\beta^2}\Bigg[&\left(1-\beta^2\right)\left(\frac{\overline{\gamma_{Cu}}}{z_i - z_m} + \frac{\gamma_{Cu}\overline{z_m}}{(z_i - z_m)^2}\right) \\ &+\left(\alpha+\beta^2\right)\left(\frac{\overline{\gamma_{Cu}}}{z_i - \overline{z_m}} + \frac{\gamma_{Cu} z_m}{(z_i - \overline{z_m})^2}\right) \\ &+(1+\alpha)\beta\left(\frac{\overline{\gamma_{Cu}}}{z_i - \overline{z_m}} - \frac{\gamma_{Cu} z_m}{(z_i - \overline{z_m})^2}\right) \\ &-(\alpha-\beta)(1-\beta)\left[\left(\overline{\gamma_{Cu}} - \gamma_{Cu}\right)\frac{\overline{z_m} - z_m}{(z_i - \overline{z_m})^2} + 2\overline{\gamma_{Cu} z_m}\frac{\bar{z}_m - z_m}{(z_i - z_m)^3}\right]\end{aligned} \tag{A4}$$

whereby α, β are again Dundurs' first and second parameter [71] and:

$$\gamma_{Cu} = \frac{G_{Cu} b_{Cu} e^{i\Theta}}{2i\pi\,(1-2\nu_{Cu})} \tag{A5}$$

Appendix B

Lin and Thomson [80] derived their framework for dislocation shielding in a 2D model with dislocations being able to lie on any slip plane, *i.e.* varying contributions of the Burger's vector on the real and imaginary axis. As in the present model the emitted dislocations lie on a crack tip intersecting slip plane in the Cu phase, we can simplify the shielding terms for the *i*-the dislocations for both modes $k^{i}_{\mathrm{I,dislocation}}$, $k^{i}_{\mathrm{II,dislocation}}$ as:

$$k^{i}_{I,dislocation} = \frac{G_{Cu} b_{Cu}}{2(1-\nu_{Cu})\sqrt{2\pi r_i}}\left[\sin(\Theta)\cos(\Theta)\ \cos\left(\frac{3\Theta}{2}\right) + 2\ \sin(\Theta)\ \cos\left(\frac{\Theta}{2}\right) + \sin^2(\Theta)\ \sin\left(\frac{3\Theta}{2}\right)\right] \tag{B1}$$

$$k^{i}_{II,dislocation} = \frac{G_{Cu} b_{Cu}}{2(1-\nu_{Cu})\sqrt{2\pi r_i}}\left[2\cos(\Theta)\cos\left(\frac{\Theta}{2}\right) - \sin(\Theta)\cos(\Theta)\sin\left(\frac{3\Theta}{2}\right) + \sin^2(\Theta)\cos\left(\frac{3\Theta}{2}\right)\right] \tag{B2}$$

References

[1] M. Mirigliano, P. Milani, Electrical conduction in nanogranular cluster-assembled metallic films, Adv. Phys. X 6 (2021) 1908847, doi:10.1080/23746149.2021.1908847.

[2] C.M. Tanner, Y.-C. Perng, C. Frewin, S.E. Saddow, J.P. Chang, Electrical performance of Al2O3 gate dielectric films deposited by atomic layer deposition on 4H-SiC, Appl. Phys. Lett. 91 (2007) 203510, doi:10.1063/1.2805742.

[3] J.G. Thakare, C. Pandey, M.M. Mahapatra, R.S. Mulik, Thermal barrier coatings - a state of the art review, Met. Mater. Int. (2020), doi:10.1007/s12540-020-00705-w.

[4] M.J. Hoque, A. Günay, A. Stillwell, Y. Gurumukhi, R.C.N. Pilawa-Podgurski, N. Miljkovic, Modular heat sinks for enhanced thermal management of electronics, J. Electron. Packag. (2021) 143, doi:10.1115/1.4049294.

[5] M. Nelhiebel, R. Illing, T. Detzel, S. Wöhlert, B. Auer, S. Lanzerstorfer, M. Rogalli, W. Robl, S. Decker, J. Fugger, M. Ladurner, Effective and reliable heat management for power devices exposed to cyclic short overload pulses, Microelectron. Reliab. 53 (2013) 1745–1749, doi:10.1016/j.microrel.2013.07.123.

[6] C. Subramanian, K.N. Strafford, Review of multicomponent and multilayer coatings for tribological applications, Wear 165 (1993) 85–95, doi:10.1016/0043-1648(93)90376-w.

[7] S. Ilican, Y. Caglar, M. Caglar, F. Yakuphanoglu, Structural, optical and electrical properties of F-doped ZnO nanorod semiconductor thin films deposited by sol–gel process, Appl. Surf. Sci. 255 (2008) 2353–2359, doi:10.1016/j.apsusc.2008.07.111.

[8] J.-Q. Xi, M.F. Schubert, J.K. Kim, E.F. Schubert, M. Chen, S.-Y. Lin, W. Liu, J.A. Smart, Optical thin-film materials with low refractive index for broadband elimination of Fresnel reflection, Nat. Photonics 1 (2007) 176–179, doi:10.1038/nphoton.2007.26.

[9] J.B. Pethicai, R. Hutchings, W.C. Oliver, Hardness measurement at penetration depths as small as 20 nm, Philos, Mag. A Phys. Condens. Matter, Struct. Defects Mech. Prop. 48 (1983) 593–606, doi:10.1080/01418618308234914.

[10] G.M. Pharr, An improved technique for determining hardness and elastic modulus using load and displacement sensing indentation experiments, J. Mater. Res. 7 (1992) 1564–1583, doi:10.1557/JMR.1992.1564.

[11] M.D. Uchic, Sample dimensions influence strength and crystal plasticity, Science (80-.). 305 (2004) 986–989, doi:10.1126/science.1098993.

[12] C.P. Frick, B.G. Clark, S. Orso, A.S. Schneider, E. Arzt, Size effect on strength and strain hardening of small-scale [1 1 1] nickel compression pillars, Mater. Sci. Eng. A 489 (2008) 319–329, doi:10.1016/j.msea.2007.12.038.

[13] D. Kiener, W. Grosinger, G. Dehm, R. Pippan, A further step towards an understanding of size-dependent crystal plasticity: in situ tension experiments of miniaturized single-crystal copper samples, Acta Mater. 56 (2008) 580–592, doi:10.1016/j.actamat.2007.10.015.

[14] K.F. Murphy, L.Y. Chen, D.S. Gianola, Effect of organometallic clamp properties on the apparent diversity of tensile response of nanowires, Nanotechnology (2013) 24, doi:10.1088/0957-4484/24/23/235704.

[15] M. Alfreider, M. Meindlhumer, V. Maier-Kiener, A. Hohenwarter, D. Kiener, Extracting information from noisy data: strain mapping during dynamic in situ SEM experiments, J. Mater. Res. (2021), doi:10.1557/s43578-020-00041-0.

[16] A. Riedl, R. Daniel, M. Stefenelli, T. Schöberl, O. Kolednik, C. Mitterer, J. Keckes, A novel approach for determining fracture toughness of hard coatings on the micrometer scale, Scr. Mater. 67 (2012) 708–711, doi:10.1016/j.scriptamat.2012.06.034.

[17] J. Ast, T. Przybilla, V. Maier, K. Durst, M. Göken, Microcantilever bending experiments in NiAl - evaluation, size effects, and crack tip plasticity, J. Mater. Res. 29 (2014) 2129–2140, doi:10.1557/jmr.2014.240.

[18] G. Sernicola, T. Giovannini, P. Patel, J.R. Kermode, D.S. Balint, T. Ben Britton, F. Giuliani, In situ stable crack growth at the micron scale, Nat. Commun. 8 (2017) 108, doi:10.1038/s41467-017-00139-w.

[19] M. Sebastiani, K.E. Johanns, E.G. Herbert, F. Carassiti, G.M. Pharr, A novel pillar indentation splitting test for measuring fracture toughness of thin ceramic coatings, Philos. Mag. 95 (2015) 1928–1944, doi:10.1080/14786435.2014.913110.

[20] M. Meindlhumer, J. Zalesak, R. Pitonak, J. Todt, B. Sartory, M. Burghammer, A. Stark, N. Schell, R. Daniel, J.F. Keckes, M. Lessiak, A. Köpf, R. Weißenbacher, J. Keckes, Biomimetic hard and tough nanoceramic Ti-Al-N film with self-assembled six-level hierarchy, Nanoscale 11 (2019) 7986–7995, doi:10.1039/c8nr10339a.

[21] D.E.J. Armstrong, M.E. Rogers, S.G. Roberts, Micromechanical testing of stress corrosion cracking of individual grain boundaries, Scr. Mater. 61 (2009) 741–743, doi:10.1016/j.scriptamat.2009.06.017.

[22] D. Kupka, E.T. Lilleodden, Mechanical testing of solid-solid interfaces at the microscale, Exp. Mech. 52 (2012) 649–658, doi:10.1007/s11340-011-9530-z.

[23] K. Matoy, T. Detzel, M. Müller, C. Motz, G. Dehm, Interface fracture properties of thin films studied by using the micro-cantilever deflection technique, Surf. Coatings Technol. 204 (2009) 878–881, doi:10.1016/j.surfcoat.2009.09.013.

[24] J. Schaufler, C. Schmid, K. Durst, M. Göken, Determination of the interfacial strength and fracture toughness of a-C:H coatings by in-situ microcantilever bending, Thin. Solid. Films 522 (2012) 480–484, doi:10.1016/j.tsf.2012.08.031.

[25] R. Konetschnik, R. Daniel, R. Brunner, D. Kiener, Selective interface toughness measurements of layered thin films, AIP Adv 7 (2017) 35307, doi:10.1063/1.4978337.

[26] G. Žagar, V. Pejchal, M.G. Mueller, L. Michelet, A. Mortensen, Fracture toughness measurement in fused quartz using triangular chevron-notched microcantilevers, Scr. Mater. 112 (2016) 132–135, doi:10.1016/j.scriptamat.2015.09.032.

[27] T. Glechner, S. Lang, R. Hahn, M. Alfreider, V. Moraes, D. Primetzhofer, J. Ramm, S. Kolozsvári, D. Kiener, H. Riedl, Correlation between fracture characteristics and valence electron concentration of sputtered Hf-C-N based thin films, 399 (n.d.) 2022 126212. doi:10.1016/j.surfcoat.2020.126212.

[28] S. Wurster, C. Motz, R. Pippan, Characterization of the fracture toughness of micro-sized tungsten single crystal notched specimen, Philos. Mag. 92 (2012) 1–23, doi:10.1080/14786435.2012.658449.

[29] J. Ast, B. Merle, K. Durst, M. Göken, Fracture toughness evaluation of NiAl single crystals by microcantilevers - a new continuous J-integral method, J. Mater. Res. 31 (2016) 3786–3794, doi:10.1557/jmr.2016.393.

[30] M. Alfreider, D. Kozic, O. Kolednik, D. Kiener, In-situ elastic-plastic fracture mechanics on the microscale by means of continuous dynamical testing, Mater. Des. 148 (2018) 177–187, doi:10.1016/j.matdes.2018.03.051.

[31] A. Wimmer, M. Smolka, W. Heinz, T. Detzel, W. Robl, C. Motz, V. Eyert, E. Wimmer, F. Jahnel, R. Treichler, G. Dehm, Temperature dependent transition of intragranular plastic to intergranular brittle failure in electrodeposited Cu microtensile samples, Mater. Sci. Eng. A 618 (2014) 398–405, doi:10.1016/j.msea.2014.09.029.

[32] S. Bigl, S. Wurster, M.J. Cordill, D. Kiener, Advanced characterisation of thermomechanical fatigue mechanisms of different copper film systems for wafer metallizations, Thin. Solid. Films 612 (2016) 153–164, doi:10.1016/j.tsf.2016.05.044.

[33] M. Alfreider, J. Zechner, D. Kiener, Addressing fracture properties of individual constituents within a Cu-WTi-SiOx-Si multilayer, JOM 72 (2020) 4551–4558, doi:10.1007/s11837-020-04444-6.

[34] E1820 ASTM Standard, Standard Test Method for Measurement of Fracture Toughness, West Conshohocken, USA, USA, 2013, doi:10.1520/E1820-13.Copyright.

[35] ISO 12135:2002 - metallic materials — unified method of test for the determination of quasistatic fracture toughness, 2002.

[36] J.R. Rice, P.C. Paris, J.G. Merkle, Some further results of J-integral analysis and estimates, in: J. Kaufman, J. Swedlow, H. Corten, J. Srawley, R. Heyer, E. Wessel, G. Irwin (Eds.), Prog. Flaw Growth Fract. Toughness Test., ASTM International, 1973, pp. 231–245, doi:10.1520/STP49643S.

[37] X.K. Zhu, J.A. Joyce, Review of fracture toughness (G, K, J, CTOD, CTOA) testing and standardization, Eng. Fract. Mech. 85 (2012) 1–46, doi:10.1016/j.engfracmech.2012.02.001.

[38] M. Alfreider, S. Kolitsch, S. Wurster, D. Kiener, An analytical solution for the correct determination of crack lengths via cantilever stiffness, Mater. Des. 194 (2020) 108914, doi:10.1016/j.matdes.2020.108914.

[39] C. Kalha, S. Bichelmaier, N.K. Fernando, J.V Berens, P.K. Thakur, T.-L. Lee, J.J.G. Moreno, S. Mohr, L.E. Ratcliff, M. Reisinger, J. Zechner, M. Nelhiebel, A. Regoutz, Thermal and oxidation stability of {TixW}1-x diffusion barriers investigated by soft and hard x-ray photoelectron spectroscopy, J. Appl. Phys. 129 (2021) 195302, doi:10.1063/5.0048304.

[40] C. Kalha, M. Reisinger, P.K. Thakur, T.-L. Lee, S. Venkatesan, M. Isaacs, R.G. Palgrave, J. Zechner, M. Nelhiebel, A. Regoutz, Evaluation of the thermal stability of TiW/Cu heterojunctions using a combined SXPS and HAXPES approach, (2022). http://arxiv.org/abs/2201.08074 (accessed February 20, 2022).
[41] Z. Nishiyama, X-ray investigation of the mechanism of the transformation from face centered cubic lattice to body centered cubic, Sci. Rep. Tohoku Univ. 23 (1934) 637.
[42] G. Wassermann, Ueber den Mechanismus der [alpha]-[gamma]-Umwandlung des Eisens, Verlag Stahleisen, 1935.
[43] G. Kresse, J. Hafner, Ab initio molecular dynamics for liquid metals, Phys. Rev. B 47 (1993) 558–561, doi:10.1103/PhysRevB.47.558.
[44] G. Kresse, J. Hafner, Ab initio molecular-dynamics simulation of the liquid-metal–amorphous-semiconductor transition in germanium, Phys. Rev. B 49 (1994) 14251–14269, doi:10.1103/PhysRevB.49.14251.
[45] G. Kresse, J. Furthmüller, Efficiency of ab-initio total energy calculations for metals and semiconductors using a plane-wave basis set, Comput. Mater. Sci. 6 (1996) 15–50, doi:10.1016/0927-0256(96)00008-0.
[46] J.P. Perdew, K. Burke, M. Ernzerhof, Generalized gradient approximation made simple, Phys. Rev. Lett. 77 (1996) 3865–3868, doi:10.1103/PhysRevLett.77.3865.
[47] J.P. Perdew, K. Burke, M. Ernzerhof, Generalized gradient approximation made simple [Phys. Rev. Lett. 77, 3865 (1996)], Phys. Rev. Lett. 78 (1997) 1396 –1396, doi:10.1103/PhysRevLett.78.1396.
[48] P.E. Blöchl, Projector augmented-wave method, Phys. Rev. B. 50 (1994) 17953–17979, doi:10.1103/PhysRevB.50.17953.
[49] G. Kresse, D. Joubert, From ultrasoft pseudopotentials to the projector augmented-wave method, Phys. Rev. B 59 (1999) 1758–1775, doi:10.1103/PhysRevB.59.1758.
[50] A.M. Tahir, R. Janisch, A. Hartmaier, Ab initiocalculation of traction separation laws for a grain boundary in molybdenum with segregated C impurites, Model. Simul. Mater. Sci. Eng. 21 (2013) 75005, doi:10.1088/0965-0393/21/7/075005.
[51] V. Tvergaard, J.W. Hutchinson, The relation between crack growth resistance and fracture process parameters in elastic-plastic solids, J. Mech. Phys. Solids. 40 (1992) 1377–1397, doi:10.1016/0022-5096(92)90020-3.
[52] T.L. Anderson, Fracture Mechanics: Fundamentals and Applications, Second Edition, CRC Press, 2005.
[53] J.H. Rose, J.R. Smith, J. Ferrante, Universal features of bonding in metals, Phys. Rev. B 28 (1983) 1835–1845, doi:10.1103/physrevb.28.1835.
[54] N.D. Ashcroft, N.W. Mermin, Solid State Physics, Harcourt College Publishers, 1976.
[55] D. Scheiber, V.I. Razumovskiy, P. Puschnig, R. Pippan, L. Romaner, Ab initio description of segregation and cohesion of grain boundaries in W–25 at.% Re alloys, Acta Mater. 88 (2015) 180–189, doi:10.1016/j.actamat.2014.12.053.
[56] M.L. Jokl, V. Vitek, C.J. McMahon, A microscopic theory of brittle fracture in deformable solids: a relation between ideal work to fracture and plastic work, Acta Metall. 28 (1980) 1479–1488, doi:10.1016/0001-6160(80)90048-6.
[57] E. Orowan, Notch brittleness and the strength of metals, Trans. Inst. Eng. Shipbuild. Scotl. 89 (1945) 165–215.
[58] A.A. Griffith, VI. The phenomena of rupture and flow in solids, Philos. Trans. R. Soc. London. Ser. A, Contain. Pap. a Math. or Phys. Charact. 221 (1921) 163–198, doi:10.1098/rsta.1921.0006.
[59] R.A. Mulford, C.J. Mcmahon, D.P. Pope, H.C. Feng, Temper embrittlement of Ni-Cr Steels by phosphorus, Metall. Trans. A 7 (1976) 1183–1195, doi:10.1007/BF02656602.
[60] T. Meiners, Z. Peng, B. Gault, C.H. Liebscher, G. Dehm, Sulfur – induced embrittlement in high-purity, polycrystalline copper, Acta Mater. 156 (2018) 64–75, doi:10.1016/j.actamat.2018.06.013.
[61] D. Mordehai, Y. Ashkenazy, I. Kelson, G. Makov, Dynamic properties of screw dislocations in Cu: a molecular dynamics study, Phys. Rev. B (2003) 67, doi:10.1103/physrevb.67.024112.
[62] E. Oren, E. Yahel, G. Makov, Dislocation kinematics: a molecular dynamics study in Cu, Model. Simul. Mater. Sci. Eng. 25 (2016) 25002, doi:10.1088/1361-651x/aa52a7.
[63] K. Marukawa, Dislocation motion in copper single crystals, J. Phys. Soc. Jpn. 22 (1967) 499–510, doi:10.1143/jpsj.22.499.
[64] A.C. Hindmarsh, L.R. Petzold, Algorithms and software for ordinary differential equations and differential- algebraic equations, Part II: higher-order methods and software packages, Comput. Phys. 9 (1995) 148, doi:10.1063/1.168540.
[65] W. Zielinski, M.J. Lii, W.W. Gerberich, Crack-tip dislocation emission arrangements for equilibrium —I. In situ TEM observations of Fe2wt%Si, Acta Metall. Mater 40 (1992) 2861–2871, doi:10.1016/0956-7151(92)90451-J.
[66] S.M. Ohr, An electron microscope study of crack tip deformation and its impact on the dislocation theory of fracture, 72 (n.d.) 2022 1–35. doi:10.1016/0025-5416(85)90064-3.
[67] C.S. Pande, R.A. Masumura, Y.T. Chou, Shielding of crack tips by inclined pile-ups of dislocations, Acta Metall. 36 (1988) 49–54, doi:10.1016/0001-6160(88)90027-2.
[68] R. Goswami, C.S. Pande, Crack-dislocation interactions ahead of a crack tip, in: Handb. Mech. Mater., Springer, Singapore, 2018, pp. 1–21, doi:10.1007/978-981-10-6855-3_52-1.
[69] M. Peach, J.S. Koehler, The forces exerted on dislocations and the stress fields produced by them, Phys. Rev. 80 (1950) 436–439, doi:10.1103/PhysRev.80.436.
[70] J.W. Hutchinson, Z. Suo, Mixed mode cracking in layered materials, in: Adv. Appl. Mech., Elsevier, 1991, pp. 63–191, doi:10.1016/S0065-2156(08)70164-9.
[71] J. Dundurs, Elastic interaction of dislocations with inhomogeneities, in: T. Mura (Ed.), Math. Theory Dislocations, ASME, 1969, pp. 70–115.
[72] R. Lowrie, A.M. Gonas, Dynamic elastic properties of polycrystalline tungsten, 24°–1800°C, J. Appl. Phys. 36 (1965) 2189–2192, doi:10.1063/1.1714447.
[73] H.M. Ledbetter, E.R. Naimon, Elastic properties of metals and alloys. {II}. Copper, 3 (n.d.) 2022 897–935. doi:10.1063/1.3253150.
[74] J. Weertman, Dislocation Based Fracture Mechanics, World Scientific Pub Co Inc, 1996.
[75] Y. Wang, W. Wang, B. Zhang, C.-Q. Li, A review on mixed mode fracture of metals, Eng. Fract. Mech. 235 (2020) 107126, doi:10.1016/j.engfracmech.2020.107126.
[76] T.-Y. Zhang, J.C.M. Li, Interaction of an edge dislocation with an interfacial crack, J. Appl. Phys. 72 (1992) 2215–2226, doi:10.1063/1.351614.
[77] N.I. Muskhelishvili, Basic equations of the plane theory of elasticity, in: Some Basic Probl. Math. Theory Elast., Springer Netherlands, 1977, pp. 89–104, doi:10.1007/978-94-017-3034-1_4.
[78] F.R.N. Nabarro, Fifty-year study of the Peierls-Nabarro stress, Mater. Sci. Eng. A 234–236 (1997) 67–76, doi:10.1016/s0921-5093(97)00184-6.
[79] Y. Kamimura, K. Edagawa, S. Takeuchi, Experimental evaluation of the Peierls stresses in a variety of crystals and their relation to the crystal structure, Acta Mater. 61 (2013) 294–309, doi:10.1016/j.actamat.2012.09.059.
[80] I.-H. Lin, R. Thomson, Cleavage, dislocation emission, and shielding for cracks under general loading, Acta Metall. 34 (1986) 187–206, doi:10.1016/0001-6160(86)90191-4.
[81] A.S. Argon, Strenghtening Mechanisms in Crystal Plasticity, Oxford University Press, 2022 n.d..
[82] U. Messerschmidt, Dislocation dynamics During Plastic Deformation, Springer, 2010.
[83] R. Maaß, P.M. Derlet, Micro-plasticity and recent insights from intermittent and small-scale plasticity, Acta Mater. 143 (2018) 338–363, doi:10.1016/j.actamat.2017.06.023.
[84] C. Motz, T. Schöberl, R. Pippan, Mechanical properties of micro-sized copper bending beams machined by the focused ion beam technique, Acta Mater. 53 (2005) 4269–4279, doi:10.1016/j.actamat.2005.05.036.